

# Excitation and RF Field Control of a Human-Size 10.5-T MRI System

Patrick Bluem<sup>ID</sup>, *Graduate Student Member, IEEE*, Pierre-Francois Van de Moortele, Gregor Adriany, *Member, IEEE*, and Zoya Popović, *Fellow, IEEE*

**Abstract**—This paper presents an investigation of methods for improving homogeneity inside various dielectric phantoms situated in a 10.5-T human-sized magnetic resonance imaging. The transmit  $B_1$  ( $B_1^+$ ) field is excited with a quadrature-fed circular patch probe and a 12-element capacitively loaded microstrip array. Both simulations and measurements show improved homogeneity in a cylindrical water phantom, an inhomogeneous phantom (pineapple), and a NIST standard phantom. The simulations are performed using a full-wave finite-difference time-domain solver (Sim4Life) in order to find the  $B_1^+$  field distribution and compared to the gradient-recalled echo image and efficiency result. For additional field uniformity, the wall electromagnetic boundary conditions are modified with a passive quadrifilar helix. Finally, these methods are applied in simulation to head imaging of an anatomically correct human body model (Duke, IT'IS Virtual Population) showing improved homogeneity and specific absorption rate for various excitations.

**Index Terms**—Finite-difference time domain (FDTD), magnetic resonance imaging (MRI), patch antenna, waveguide.

## I. INTRODUCTION

MAGNETIC resonance imaging (MRI) at ultra-high magnetic field ( $B_0 > 7$  T) can increase signal-to-noise ratio (SNR) [1], improve spatial resolution [2], [3], provide better parallel imaging performance [4], and improve contrast [4]. Since the magnetic field strength is directly proportional to the spin precession frequency ( $\gamma = 42.58$  MHz/T for hydrogen proton imaging), at  $B_0 = 10.5$  T, the resulting wavelength in water is about 7.5 cm, which is significantly smaller than the field of view. A standard water phantom used in MRI research is a cylinder with a 16-cm diameter that can support standing waves, resulting in peaks and nulls in the applied RF right-handed circular polarized magnetic flux density ( $B_1^+$ ),

Manuscript received August 6, 2018; revised October 26, 2018; accepted November 4, 2018. Date of publication December 14, 2018; date of current version March 5, 2019. This work was supported in part by the National Science Foundation under a Collaborative Research Grant ECCS 1307614 at the University of Colorado, Boulder, and in part by the National Institutes of Health under Grant P41 EB015894 and Grant S10 RR029672. (*Corresponding author: Patrick Bluem.*)

P. Bluem and Z. Popović are with the Department of Electrical, Computer and Energy Engineering, University of Colorado, Boulder, CO 80309-0425 USA (e-mail: patrick.bluem@colorado.edu; zoya.popovic@colorado.edu).

P.-F. Van de Moortele and G. Adriany are with the Center for Magnetic Resonance Research, Department of Radiology, University of Minnesota, Minneapolis, MN 55455 USA.

Color versions of one or more of the figures in this paper are available online at <http://ieeexplore.ieee.org>.

Digital Object Identifier 10.1109/TMTT.2018.2884405

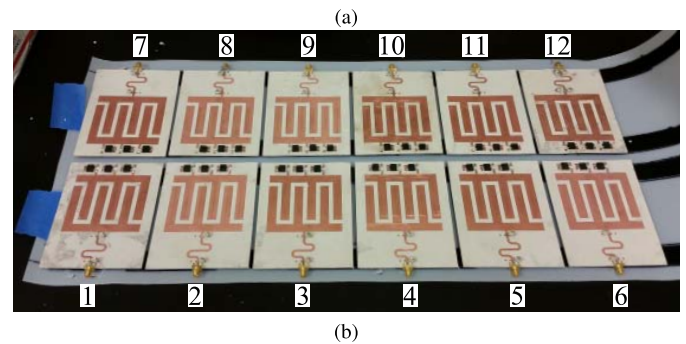
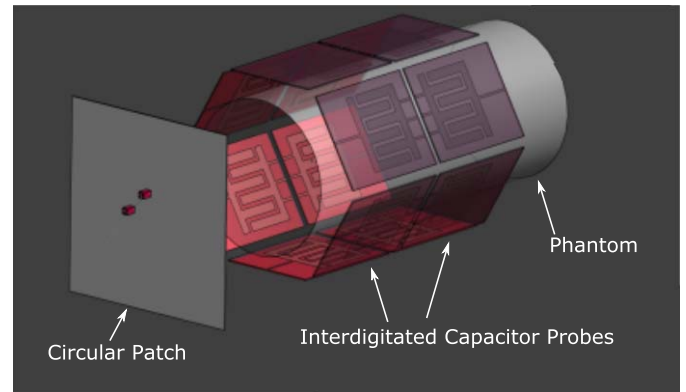


Fig. 1. (a) Simulation setup (Sim4Life) showing cylindrical phantom surrounded by interdigitated capacitor probe array with patch probe excitation. (b) Fabricated interdigitated capacitor probe array.

which corresponds to the transmit  $B_1$  field in MRI. Additionally, the wide bore desired for human imaging has a spatially complex electromagnetic (EM) field distribution, in contrast to lower field quasi-static coil excitations.

The high Larmor frequency requires different excitations compared to those at lower magnetic fields ( $B_0 < 3$  T). Current 7-T transmit schemes include dipoles [5], combination of loops and dipoles with magnetic wall filters [6], microstrip radiators [7]–[9], standard patch antennas [10]–[13], and coaxial waveguide [14]. The shorter wavelength at 10.5 T results in a smaller excitation probe that can impedance matched to 50 ohms when placed in the loaded bore, such as those shown in Fig. 1. For improved spatial coverage in ultra-high field systems, microstrip arrays (see [8]) replace the quasi-static bird cage excitation of lower field systems. With array excitations, high isolation is challenging to obtain due to the close proximity of the elements. The decrease in

wavelength at 10.5 T assists in this effort with a 3-dB lower coupling coefficient at similar physical spacing compared to 7 T [15].

In this paper, we address the problem of inhomogeneous  $B_1^+$  in the imaging volume due to complex field profiles associated with the electrically large size of the bore and imaging volume. Excitation geometries and passive EM structures that can modify the field profiles and improve field uniformity are investigated in simulations and measurement. Due to the complex nature of the fields inside of the imaging volume, these are not a complete solution, but instead present a study on possible ways to improve homogeneity inside of a uniform phantom, the worst case scenario. Excitation probes are designed using full-wave EM analysis and experimentally validated and quantified in a human-size 90-cm-diameter 10.5-T Siemens scanner at the University of Minnesota Center for Magnetic Resonance Research (CMRR) using a homogeneous water phantom ( $\epsilon_r = 81$ ,  $\sigma_d = 0.4$ ). We show that nonuniform imaging volumes, such as a NIST phantom and a pineapple, inherently have improved  $B_1^+$  field uniformity. After the probe and passive field modifier designs are validated, simulations are performed with an anatomically accurate human model from the ITIS virtual population. A distribution comparison is presented in terms of  $B_1^+$  and specific absorption rate (SAR) in the imaging volume.

This paper outline is as follows. Section II shows the system configuration, probe design and excitation scheme, and different phantom wall boundary field modifier structures. Sections III and IV quantify the water phantom simulations and experiments. The water phantom is the worst case scenario in terms of homogenizing the  $B_1^+$  field due to resonances inside of the phantom. Section VI explores the use of two inhomogeneous imaging volumes, NIST phantom (similar to [16]) and pineapple, to highlight the differences with a homogeneous water phantom. Section VII uses an anatomically correct human body model from the Virtual Population developed by ITIS (Zürich, Switzerland) to show how the demonstrated probes and additional conductive structures that modify the EM fields can be used to develop a head excitation scheme.

## II. SYSTEM CONFIGURATION

The overall system configuration is described in Fig. 2(a). MR experiments were collected at the CMRR, on a prototype 90-cm-diameter whole-body MR scanner (Siemens, Erlangen, Germany) operating at 10.5 T, equipped with an insert body gradient coil of 67 cm inner diameter as shown in Fig. 2(a). The gradient coil is 125 cm long with a spherical encoding region of about 40 cm in diameter, cogenerated with the magnet isocenter. The complete length of the bore is 443 cm. The metal bore is a circular waveguide where the unloaded cutoff frequency of the fundamental  $TE_{11}$  mode is given by [17]

$$f = \frac{0.293}{a\sqrt{\mu\epsilon}} = 262.4 \text{ MHz} \quad (1)$$

where  $a$  is the radius under the gradient coil equal to 67 cm. Without loading, the gradient coil supports three propagating modes. When loaded with a high dielectric constant volume,

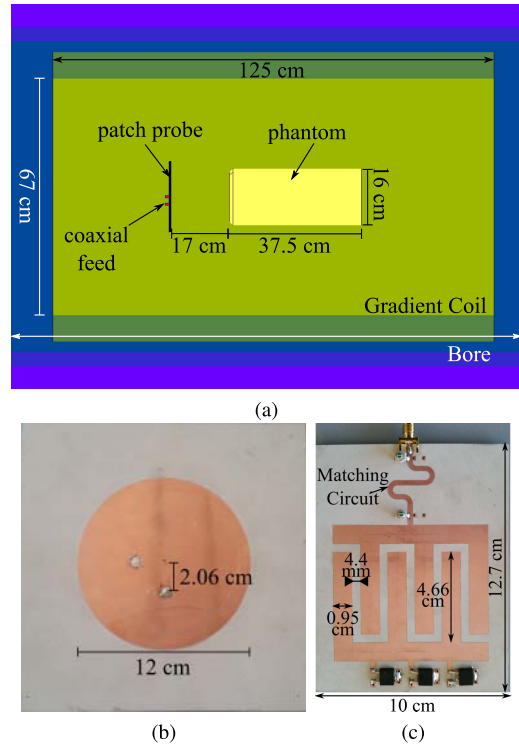


Fig. 2. (a) Dimensions of the 10.5-T Siemens scanner with cylindrical phantom shown from the side. (b) Coaxially quadrature-fed circular patch probe. (c) Interdigitated capacitor probe designed for 447 MHz.

the number of propagating modes increases, complicating the homogenization of the imaging volume.

The necessary RF spin excitation frequency is given as

$$f = \gamma B_0 \quad (2)$$

where  $\gamma$  is the gyromagnetic ratio of the  $H^1$  nucleus, 42.58 MHz/T, and  $B_0$  is the dc magnetic field of 10.5 T. The increase in excitation frequency to 447 MHz, compared to clinical scanners at 1.5 T (68 MHz) and 3 T (127 MHz), reduces the wavelength inside of the imaging volume. The imaging volume becomes electrically large and standing waves develop in contrast to the traditional quasi-static approximation used to design RF coils. The dielectric phantom used in experiments is the Siemens 55 12 608 K2205 with 16 cm diameter and 37.5 cm length. The phantom is filled with DI water of  $\epsilon_r = 81$  and  $\sigma_d = 0.4$  S/m.

The RF portion of the MR system includes up to 32 receive channels as well as 16 independent transmit RF channels allowing for different transmit RF phases for each of the individual RF elements. A specific set of relative transmit RF phases is referred to as  $B_1$  shimming. Each RF channel is powered by a 1-kW RF amplifier. Any RF coil element could be utilized during both RF transmission and signal reception using a multichannel T/R switch board built at CMRR.

Two imaging protocols were used for images reported here:  $|B_1^+|$  mapping and conventional gradient echo images (GREs).  $|B_1^+|$  maps were obtained with the 3-D actual flip angle (AFI) technique [18]. It should be noted that wherever receive or transmit local  $B_1$  fields are very weak,  $|B_1^+|$  may not be

measurable because of either limited SNR or too small flip angle. Thus, it is typical to obtain patchy measured  $|B_1^+|$  maps at very high fields in a dielectric phantom. Conventional GRE images were collected in a relatively small flip angle regime, a condition where image intensity is typically proportional to the product of the magnitude transmit  $B_1$  field and the square root of sum of squares of the 12 magnitudes of the receive  $B_1$  fields.

For phantom experiments, the sets of relative RF phases (i.e.,  $B_1$  shimming) applied to the transmit channels were defined based on EM simulations conducted in Sim4Life (see corresponding tables throughout this paper).

For data obtained in a pineapple with its long axis parallel to the longitudinal  $B_0$  axis, an additional imaging protocol was used to obtain multichannel relative complex  $|B_1^+|$  map, consisting of multislice 2-D GRE image series obtained by pulsing sequentially on one transmit channel at a time while receiving on all receive channels [19], [20].  $B_1$  shimming was then performed in an region of interest elongated along the  $z$ -axis covering the central core of the pineapple with an algorithm aiming at maximizing constructive interferences between the complex  $|B_1^+|$  field of all transmit coils [21].

In all experiments,  $B_1$  shimming was applied by only varying relative transmit RF phases between channels.

#### A. Circular Patch Probe

A quadrature circular patch is an effective traveling-wave MR probe [11]. The circular spatial current density distribution on the probe excites a circularly polarized field in the cylindrical bore as shown in [22]. A similar coaxially fed patch is designed on a Rogers 3010 substrate,  $\epsilon_r = 11.2$  and 1.27 mm thick, shown in Fig. 2(b). The probe is designed with no additional matching circuit and has a return loss greater than 15 dB over a 10-MHz bandwidth. Its diameter is 12.28 cm and the feeds are spaced 2.06 cm from the center of the patch to maintain a low axial ratio and high return loss. In free space, the probe is a well-matched resonant patch antenna. The return loss remains high when the probe is inside the electrically large bore at this frequency, since it is placed at a reasonable distance from the imaging volume,  $> 10$  cm and is, therefore, not heavily loaded. The ground plane is cut to a 20 cm  $\times$  20 cm square to align the center of the patch with the phantom. The coaxial quadrature feed allows phase and amplitude scaling of the feeds for either sense (right or left) of circular polarization and  $B_1$  shimming. Referring to Fig. 2(a), 17 cm distance from the dielectric phantom is a tradeoff between the circular polarization quality and excitation field magnitude.

#### B. Interdigitated Capacitor Probe

Traveling-wave excitations have poor spatial coverage of the imaging volume, reducing the overall signal level coupled back into the probe for the received image. An interdigitated capacitor probe [23] is created to improve on this major drawback [Fig. 2(c)]. This probe is designed on Rogers 6010,  $\epsilon_r = 10.6$ , 1.27-mm-thick substrate. The finger dimensions are chosen to ensure uniform current distribution across the

two middle fingers while maintaining a high return loss. The combination of the number of fingers and finger width will affect the loading and current distribution on each finger. The design is chosen to target the loading to create a balanced current distribution on the inner two fingers. The interdigitated capacitor probe is a traveling-wave probe, and as such needs appropriate resistive loading to eliminate a standing wave across the probe. Reactive loading can also be used [24] but is prohibitively large for this application and the number of radiating elements. Simulations show that a 25- $\Omega$  load would allow 30% of the power to be dissipated in the load. Instead of a single resistor, three 75- $\Omega$  resistors are used to satisfy the traveling-wave condition while balancing the current across the three pairs of fingers. Simulations also showed that adequate loading for probes could be accomplished by using the high-permittivity imaging volume as the primary load and that the resistors had little overall impact on the current distribution. Since the primary goals of this paper are the development of boundary structures for improving field homogeneity for the transmitted  $B_1^+$ , the resistors are kept in order to reduce the number of experimental variables, at the cost of increased noise.

The Rogers 6010 substrate exhibits a substantial anisotropic variation in permittivity across the 12.7 cm  $\times$  12.7 cm panel. To compensate for this unknown variation, a  $\Pi$  matching network is designed using two 250-V shunt mechanically variable capacitors and a length of line shown in Fig. 2(c). The variable capacitors are tuned to have a narrowband frequency response where the return loss is greater than 15 dB at 447 MHz.

12 interdigitated capacitor probes are wrapped 60° apart and in two rows (or rings) around the dielectric phantom, as shown in Fig. 1(a). Simulating this electrically large structure presents some issues. For example, since finite-difference time-domain (FDTD) solvers require rectangular voxels, the diagonal interdigitated capacitor probes are meshed incorrectly. Regardless of the mesh size, the top radiating copper layer is overapproximated or underapproximated and the results become inaccurate. With a near-field excitation, the currents along the radiating element greatly affect the resulting field. To alleviate this issue, each probe is aligned with the mesh, and the domain is rotated around the probe. This ensures proper meshing of each radiating element and the resulting field can then be scaled, phased, and recombined using superposition to determine the overall field excitation. The FDTD solver, Sim4Life, is chosen in particular due to the ease of use with an anatomically correct human body model and electrical parameters for the given excitation frequency. A single HFSS simulation determines the coupling between the 12 probes is less than  $-30$  dB in the worst case for each element. Simulations show this is due to the close vicinity of the high-permittivity dielectric.

### III. PROBE VALIDATION WITH WATER PHANTOM

The first experimental validation is performed with probes to evaluate the accuracy of full-wave FDTD simulations. Specifically, simulated  $|B_1^+|$  transmit efficiency is compared

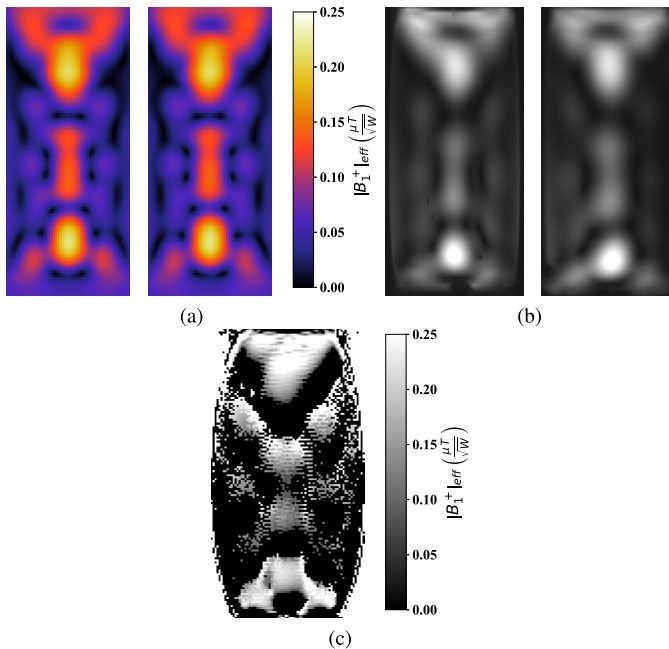


Fig. 3. Single circular patch probe: coronal (left) and sagittal (right). (a) Simulated  $|B_1^+|$  efficiency. (b) Measured GRE images. (c) Measured  $|B_1^+|$  efficiency inside of cylindrical phantom. Geometric distortions (barreling aspect) of  $|B_1^+|$  are due to uncorrected nonlinearity of the gradient coils.

qualitatively to the GRE images and quantitatively to measured  $|B_1^+|$  maps with the Siemens 10.5-T scanner using the standard water phantom. The efficiency of the experimental results is expected to be lower than simulations because excitation power is not calibrated to the connection of the probe elements. Additionally, some black holes in the plots are due to miscalibrations of the scanner.

#### A. Circular Patch Probe

Referring to Fig. 2(a), the patch is placed 17 cm away from the phantom and the two feeds are excited in quadrature, or  $90^\circ$  out of phase, and with an equal power. Either circular polarization can be excited by varying the relative  $90^\circ$  phase difference. The phantom is placed in the isocenter of the bore and excited with an absolute flip angle imaging (AFI) sequence. Fig. 3 shows the results with the single circular patch probe. The efficiency, in  $\mu\text{ T}/\sqrt{W}$ , from the simulation in Fig. 3(a) correlates well with the experimental result in Fig. 3(b) and (c). Due to system imperfections and very low SNR in  $|B_1^+|$  maps in locations where  $|B_1^+|$  is weak, the exact excitation magnitude and phase will vary slightly from the desired value. For this experiment, the variations are fairly low and the experimental result is similar to the simulated result shown in Fig. 3(a). The absolute  $|B_1^+|$  map can be seen in Fig. 3(c) to also have good agreement with the simulated response. The magnitude of the efficiency map is slightly higher than expected due to the uncorrected geometric distortion.

The efficiency is calculated on the coronal slice as the AFI sequence images coronal cuts and, therefore, only one cross section is shown. Agreement between the efficiency map and

experimental image is expected in this case as the transmit and receive profiles of the single patch probe experiment should be similar by reciprocity because the left- and right-handed circular polarizations are identical. With more complicated excitations, which are phased relative to each other, this will not be the case and the simulation should correlate with the efficiency map and vary slightly from the GRE images. As the GRE images are approximately proportional to the product of the transmit and receive profiles, their spatial pattern can vary and may have limited consistency with transmit  $B_1$  simulation.

#### B. Interdigitated Capacitor Probe Array

To improve the spatial distribution around the phantom and the field distribution inside of the phantom, a volume excitation system is created from interdigitated capacitors. Two rows (or rings) of six probes are wrapped around the phantom as shown in Fig. 1(a) for a total of 12 additional excited ports compared to the circular patch probe setup. With the correct sequential phasing, the array can transmit either circular polarization. The field distribution can additionally be improved by varying the magnitudes and phases of individual element. For all plots in the following sections, the coronal slice is shown on the left and the sagittal on the right.

The interdigitated capacitor probe array [Fig. 1(b)] is held in place using 0.5-mm plastic with hook and loop fasteners for flexibility. The probes are placed 3 cm from the phantom to ensure minimal coupling between the elements. The probes are initially simulated and measured separately with a  $60^\circ$  sequential phase difference around the phantom to achieve circular polarization. The probes are excited with the same magnitude to reduce the number of variables when comparing to simulations, as each excitation port has a small magnitude and phase variation from the mean. Fig. 4 shows the expected result using Sim4Life and the experimental result. The efficiency result in Fig. 4(c) is expectedly low as it is the center coronal slice, between two probe elements

#### C. Combining the Two Probes

Combining the interdigitated capacitor array with the traveling-wave circular patch can improve the overall field distribution to a targeted region of interest inside the phantom. The relative phasing that minimizes the change in  $|B_1^+|$  is found using a least-squares algorithm. The two goal functions are defined as

$$\min \frac{|\nabla |B_1^+||}{\mu |B_1^+|} \text{ and } \min \frac{\sigma |B_1^+|}{\mu |B_1^+|} \quad (3)$$

where  $\mu$  and  $\sigma$  are the mean and standard deviation of  $|B_1^+|$ . Because the variation of the power amplifiers, T/R switch modules, and over path length is not calibrated, only the relative phasing is modified in order to reduce the number of variables to compare the results to simulations. For all practical purposes, the system is capable of varying relative amplitudes between channels. For the phantom results, the region of interest is a 14-cm-wide cylinder covering all but the edges of the phantom. While such a large region might

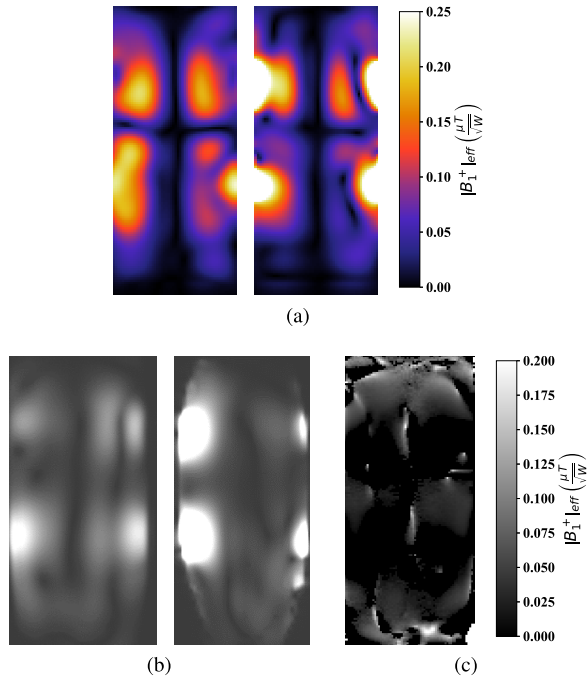


Fig. 4. Interdigitated capacitor probe array: coronal (left) and sagittal (right). (a) Simulated  $|B_1^+|$  efficiency. (b) Measured GRE images. (c) Measured  $|B_1^+|$  efficiency inside of cylindrical phantom.  $60^\circ$  incremental phasing with equal magnitude excitation on the interdigitated capacitor probes. Geometric distortions (barreling aspect) of  $|B_1^+|$  are due to uncorrected nonlinearity of the gradient coils.

be unrealistic, it illustrates clearly the differences between the various excitation schemes.

Combining the two approaches increases the overall efficiency in the areas of interest. Even though the overall excitation power increases, the peak magnitude does not increase substantially. The location of the array is chosen to improve the excited field distribution. The phases chosen to excite the array relative to the patch phase are shown in Table I, with the probe order in Fig. 1(b). The magnitude of the excitation is set to 25% of the patch excitation magnitude. If the volume excitation can be placed farther from the phantom, the magnitude of the excitation can be increased to reduce the near field shown in the coronal slice. The circular patch probe is excited with the maximum amount of the power available from the RF power amplifiers and in the quadrature. The coronal slice correlates well with the simulation shown in Fig. 5(a), with minor differences due to magnitude and phase variation in the excitation and overall placement of the interdigitated capacitor array. Minor variations in the placement along the phantom's center axis can shift the excitation. This can be beneficial to complement the distribution due to the traveling-wave excitation. The sagittal slice differs slightly from the simulation as the gradient distortion is not corrected as well as the coronal slice.

#### IV. BOUNDARY CONDITION MODIFICATIONS

Due to the electrically large size of the phantom, homogenizing the excited  $|B_1^+|$  field becomes increasingly difficult for higher field systems due to the increased number of supported

TABLE I  
RELATIVE PHASE EXCITATIONS FOR THE PATCH PROBE  
AND ARRAY COMBINATION (FIG. 5)

1	2	3	4	5	6
$74^\circ$	$164^\circ$	$180^\circ$	$228^\circ$	$274^\circ$	$339^\circ$
7	8	9	10	11	12
$169^\circ$	$236^\circ$	$273^\circ$	$298^\circ$	$334^\circ$	$19^\circ$

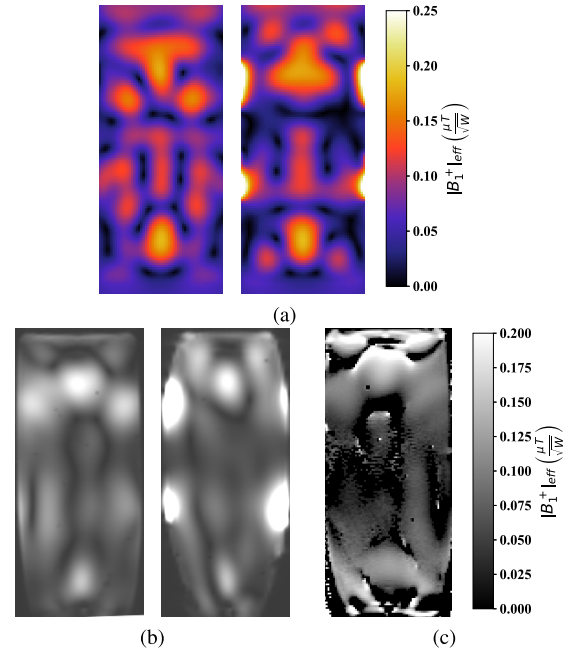


Fig. 5. Circular patch probe and interdigitated capacitor probe array: coronal (left) and sagittal (right). (a) Simulated  $|B_1^+|$  efficiency. (b) Measured GRE images. (c) Measured  $|B_1^+|$  efficiency inside of cylindrical phantom. Phasing shown in Table I and magnitude excitations, a quarter of the magnitude of the circular patch.

modes inside of the dielectric cavity. Typical  $|B_1^+|$  shimming can only partially improve the field homogeneity [15]. Additionally, the complex structure of biological tissues can further complicate the excited field profile which can be manipulated using specially designed high permittivity [25] or metallic structures [22]. Three basic passive field modifiers are explored in this paper: 1) an undriven quadrifilar helix; 2) electrically hard surfaces; and 3) electrically soft surfaces [26].

An undriven quadrifilar helix (Fig. 6) implemented with copper strips on a thin Mylar sheet is placed 3 cm from the patch, 1 cm from the phantom, 24 cm from the gradient coil, and has a 5-cm pitch. With the rotation sense following the right-handed circular polarization necessary, the helix can improve the overall efficiency in the far ends of the phantom while improving uniformity in the close end of the phantom, relative to the probe, as shown in Fig. 7. The relative phases of the probes can be seen in Table II.

It is interesting to investigate the required helix length since in some cases it may not be practical to cover the entire volume. The helix is reduced to cover  $2/3$  of the phantom, and the arms are shorted together at the far end. This allows for further homogenization without reducing efficiency, however, the result is fairly asymmetric as shown in Fig. 8. The asym-

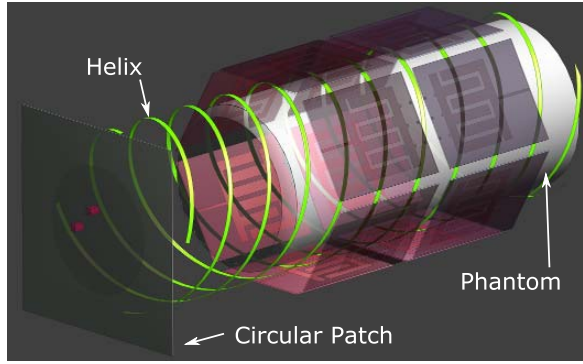


Fig. 6. Sim4Life setup with the interdigitated capacitor probe array encircling the phantom and helix boundary structure.

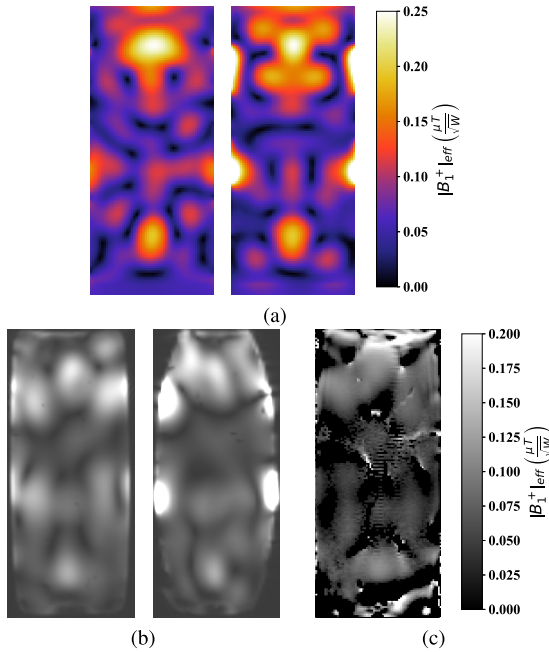


Fig. 7. Circular patch probe and interdigitated capacitor probe array with quadrifilar strip helix: coronal (left) and sagittal (right). (a) Simulated  $|B_1^+|$  efficiency. (b) Measured GRE images. (c) Measured  $|B_1^+|$  efficiency inside of cylindrical phantom. Phasing shown in Table II and magnitude excitations a quarter of the magnitude of the circular patch. Geometric distortions (barreling aspect) of  $|B_1^+|$  are due to uncorrected nonlinearity of the gradient coils.

TABLE II

RELATIVE PHASE EXCITATIONS FOR THE PATCH PROBE AND ARRAY COMBINATION WITH STRIP HELIX (FIG. 7)

<b>1</b>	<b>2</b>	<b>3</b>	<b>4</b>	<b>5</b>	<b>6</b>
119°	180°	190°	252°	291°	320°
<b>7</b>	<b>8</b>	<b>9</b>	<b>10</b>	<b>11</b>	<b>12</b>
180°	335°	24°	44°	69°	136°

metry is expected from the simulation [Fig. 8(a)]; however, the effect is more pronounced in the experimental results, possibly due to magnitudes and phases deviating slightly from simulated values. The phase excitations for the shorted helix are shown in Table III.

Other boundary structures that can affect field uniformity are electrically hard and soft surfaces as shown previously in [22].

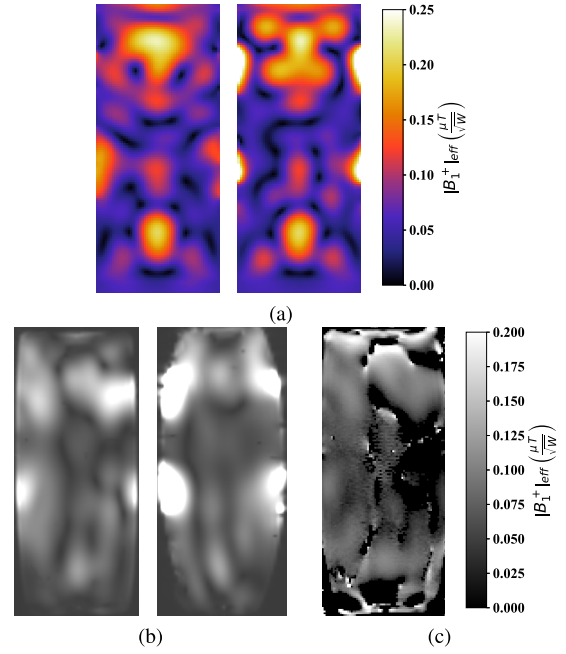


Fig. 8. Circular patch probe and interdigitated capacitor probe array with shorted quadrifilar strip helix: coronal (left) and sagittal (right). (a) Simulated  $|B_1^+|$  efficiency. (b) Measured GRE images. (c) Measured  $|B_1^+|$  efficiency inside of cylindrical phantom. Phasing shown in Table III and magnitude excitations a quarter of the magnitude of the circular patch. Geometric distortions (barreling aspect) of  $|B_1^+|$  are due to uncorrected nonlinearity of the gradient coils.

TABLE III

RELATIVE PHASE EXCITATIONS FOR THE PATCH PROBE AND ARRAY COMBINATION WITH SHORTED STRIP HELIX

<b>1</b>	<b>2</b>	<b>3</b>	<b>4</b>	<b>5</b>	<b>6</b>
116°	189°	201°	275°	297°	343°
<b>7</b>	<b>8</b>	<b>9</b>	<b>10</b>	<b>11</b>	<b>12</b>
1°	2°	30°	63°	79°	160°

Electrically hard surfaces are longitudinal corrugations used in horn antennas, to increase aperture efficiency by distributing the field more uniformly across the aperture, characterized by  $H_{lon} = 0$  along the boundary [26], [27]. Electrically soft surfaces are transverse corrugations, characterized by  $H_{tan} = 0$  along the boundary, which give zero electric field at the wall, reducing the sidelobe level and broadening the beamwidth [27]. For these experiments, electrically hard and soft surfaces are approximated with longitudinal and transverse strips, respectively, significantly reducing their size. With an approximation to an electrically hard surface covering the bottom third of the phantom, the setup in Fig. 9 and results in Fig. 10, and specifically, Fig. 10(c) shows the improved field distribution in the upper and middle regions of the phantom. The strip structure is composed of 12 15.7-cm-long strips. The longitudinal strips result in the distribution spreading in the latter portions of the phantom as shown in Fig. 10(a).

With an approximation of an electrically soft surface using seven rings of lateral strips wrapped around the circumference of the cylinder, the setup shown in Fig. 11, Fig. 12(c) shows an increase in field homogeneity in the phantom. This results

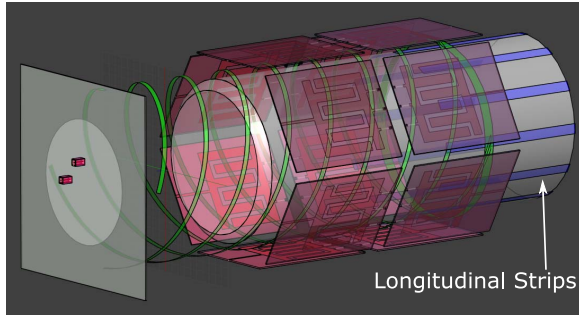


Fig. 9. 10.5-T simulation setup showing longitudinal strips approximating an electrically hard surface added to the previous setup in Fig. 6.

TABLE IV

RELATIVE PHASE EXCITATIONS FOR THE PATCH PROBE AND ARRAY COMBINATION WITH SHORTED STRIP HELIX WITH LONGITUDINAL END STRIPS (FIG. 10)

1	2	3	4	5	6
112°	166°	176°	257°	284°	310°
7	8	9	10	11	12
1°	15°	69°	103°	129°	200°

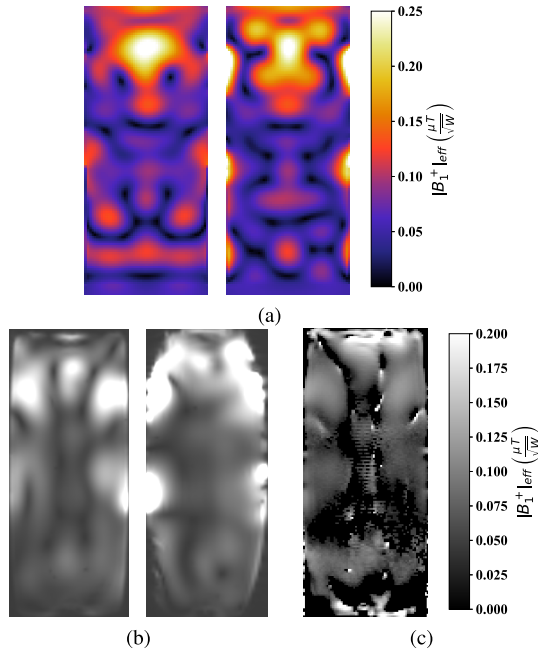


Fig. 10. Circular patch probe and interdigitated capacitor probe array with quadrifilar strip helix and longitudinal end strips: coronal (left) and sagittal (right). (a) Simulated  $|B_1^+|_{\text{eff}}$  efficiency. (b) Measured GRE images. (c) Measured  $|B_1^+|_{\text{eff}}$  efficiency inside of cylindrical phantom. Phasing shown in Table IV and magnitude excitations a quarter of the magnitude of the circular patch. Geometric distortions (barreling aspect) of  $|B_1^+|_{\text{eff}}$  are due to uncorrected nonlinearity of the gradient coils.

in a higher field amplitude in the center of the phantom as shown in Fig. 12(a). Unfortunately, metallic strips will increase the SAR along the boundary if they are placed directly on the surface. A thin dielectric can be used as an intermediate boundary layer to reduce the impact of the metallic structure at the cost of a reduced effect of the boundary structure, as is easily shown by simulations.

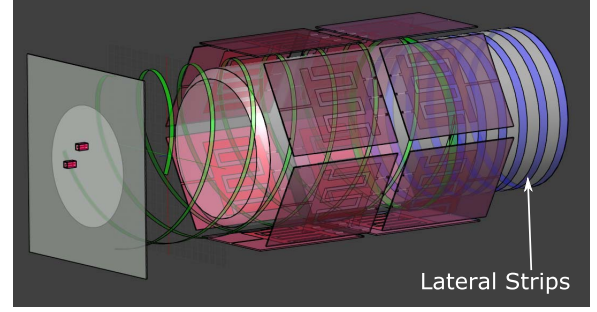


Fig. 11. Setup showing lateral strips approximating an electrically soft surface.

TABLE V

RELATIVE PHASE EXCITATIONS FOR THE PATCH PROBE AND ARRAY COMBINATION WITH SHORTED STRIP HELIX WITH LATERAL END STRIPS (FIG. 12)

1	2	3	4	5	6
1°	38°	99°	128°	152°	221°
7	8	9	10	11	12
74°	107°	188°	202°	259°	310°

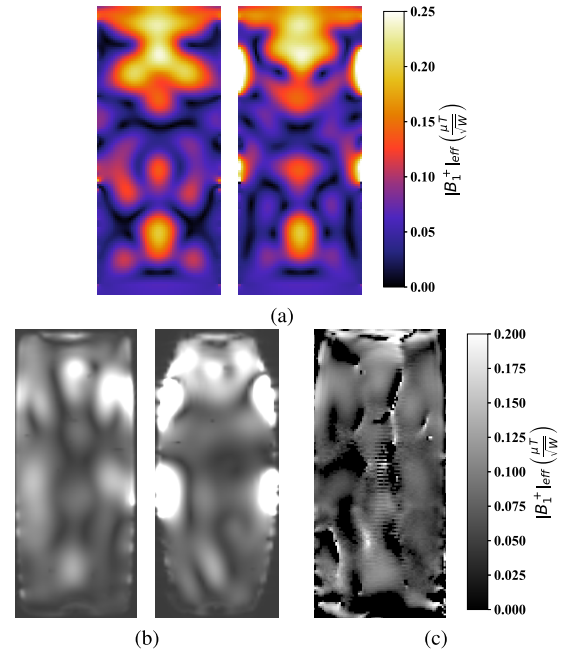


Fig. 12. Circular patch probe and interdigitated capacitor probe array with quadrifilar strip helix and lateral end strips: coronal (left) and sagittal (right). (a) Simulated  $|B_1^+|_{\text{eff}}$  efficiency. (b) Measured GRE images. (c) Measured  $|B_1^+|_{\text{eff}}$  efficiency inside of cylindrical phantom. Phasing shown in Table V and magnitude excitations a quarter of the magnitude of the circular patch. Geometric distortions (barreling aspect) of  $|B_1^+|_{\text{eff}}$  are due to uncorrected nonlinearity of the gradient coils.

## V. RESULT COMPARISON

The simulated results are compared to the experimental results using mean square error

$$\text{MSE} = \frac{1}{N} \sum_{i=1}^N (X - Y)^2 \quad (4)$$

TABLE VI  
MSE BETWEEN SIMULATION AND EXPERIMENT

Experiment	MSE Coronal (%)	MSE Sagittal (%)	Eff. Map (%)
Circular Patch Probe	1.2	1.5	8.4
Interdigital Capacitor Probe Array	3.8	3.8	16
Combination	3.6	4.8	9.7
Strip Helix	4.8	4.5	5.7
Shorted Strip Helix	5.1	7.9	6.7
Helix with End Long. Strips	5.6	8.5	7.8
Helix with End Lat. Strips	6.2	9	7

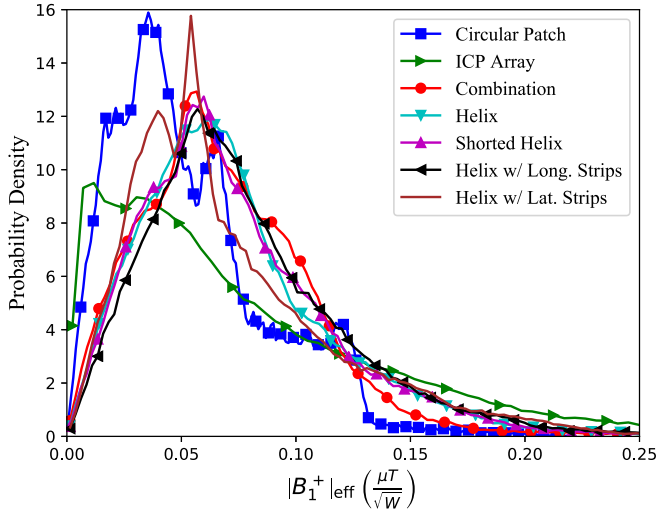


Fig. 13. Probability density of the magnitude  $B_1^+$  efficiency for various configurations. The results from the helical structure with longitudinal and lateral strips show a trend toward Gaussian behavior.

where  $X$  are the simulated and  $Y$  are the  $N$  experimental data points,  $N = 153344$ , with results in Table VI. Some minimum error is expected due to the difference between the simulated and GRE DICOM results, due to the transmit and receive multiplication, along with the sagittal slices having a large uncorrected geometric distortion. Differences between the simulated and experimental efficiency maps are generally due to regions with low SNR which are not properly mapped to an efficiency value. For this reason, the error in the interdigitated capacitor probe array experiment is large because of the oversaturation of the region closest to the probes at the center slice. Additionally, due to a slight overestimation of the circular patch probe efficiency in the combined case, the results reduce the effect of the interdigitated capacitor probe array and create additional error in the comparison. For the cleaner coronal cut results, the error stays below 7%.

A comparison of the simulated results is used to determine the effectiveness of the boundary structures the four statistical moments, mean, variance, skewness, and kurtosis based on the probability density as shown in Fig. 13 with 200 bins for 291719 points. The non-Gaussian nature of the data requires more than just mean and variance to show how the boundary structures modify the data. A positive skewness generally indicates a higher concentration above the mean.

TABLE VII

FOUR-MOMENT STATISTICAL SIMULATION COMPARISON IN ( $\mu T/\sqrt{W}$ )

Simulation	Max	Mean	Variance	Skewness	Kurtosis
Circular Patch Probe	0.22	0.054	0.0012	0.912	0.843
Interdigital Capacitor Probe Array	0.93	0.086	0.0075	2.795	12.43
Combination	0.50	0.071	0.0018	2.08	9.83
Strip Helix	0.51	0.078	0.0022	1.77	6.30
Shorted Strip Helix	0.49	0.075	0.0021	1.74	6.21
Helix with End Long. Strips	0.48	0.078	0.0022	1.61	5.17
Helix with End Lat. Strips	0.48	0.073	0.0024	1.66	4.44

TABLE VIII

NORMALIZED FOUR-MOMENT STATISTICAL EXPERIMENT COMPARISON

Experiment	Mean	Variance	Skewness	Kurtosis
Circular Patch Probe	0.47	0.19	0.054	-1.79
Interdigital Capacitor Probe Array	0.35	0.17	0.079	-1.1
Combination	0.49	0.15	0.17	-1.45
Strip Helix	0.44	0.14	0.43	-1.3
Shorted Strip Helix	0.48	0.14	0.29	-1.28
Helix with End Long. Strips	0.46	0.14	0.34	-1.31
Helix with End Lat. Strips	0.50	0.12	0.28	-1.16

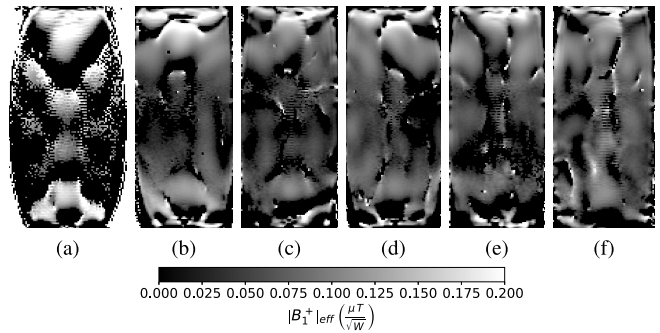


Fig. 14. Experimental efficiency comparison for (a) single patch probe, (b) combination single patch probe and interdigitated capacitor probe array, (c) strip helix, (d) shorted strip helix, (e) shorted strip helix with longitudinal end strips, and (f) strip helix with lateral end strips.

The kurtosis reported is excess kurtosis, or kurtosis centered around 0 instead of 3. An excess kurtosis below 0 implies a platykurtic distribution, focused around the mean. Ideally, the mean should be as high as possible, the skewness should be close to 0, indicating a Gaussian distribution, and the kurtosis should be as small as possible, indicating the distributions are focused toward the mean. Relative to the field produced by the circular patch probe alone (Table VII), with each field modifier, the mean is increased by 50%, at the expense of uniformity. However, by adding increasingly more complex boundary conditions, the skewness and kurtosis both decrease substantially compared to the initial approach with the combination of circular patch probe and interdigitated capacitor

TABLE IX  
RELATIVE PHASE EXCITATIONS FOR THE INHOMOGENEOUS  
IMAGING VOLUMES (FIG. 15 AND 16)

1	2	3	4	5	6
112°	313°	145°	111°	40°	335°
7	8	9	10	11	12
314°	61°	60°	99°	241°	259°

probes. The experimental analysis using the efficiency map, normalized to 1, shows a similar trend (Table VIII). With a more complex structure, the mean increases while the variance decreases, with the skewness consistently close to 0 and excess kurtosis remaining relatively consistent around  $-1.5$ . The differences in statistics can be partially attributed to a slightly modified experimental setup compared to simulation. The air capture region of the bottle prevented the helix and end strips from being perfectly circular along with some slack in the interdigitated capacitor probe construction, preventing completely equidistant excitations from each element.

A visual comparison of the plots in Fig. 14 reveals increased homogeneity with increasing hardware complexity. While these field profiles will change slightly between imaging volumes, the boundary structures will perform similarly. For example, an electrically hard surface will still act as an electrically hard surface.

As of these measurements, there is only one published work on 10.5-T MRI [15]. This paper differs from the present investigation at multiple levels, such as the design of the individual coil elements (dipoles) and the overall size and arrangement (large ellipsoid-shaped phantom), and, very importantly, the coil elements considered are positioned very closely to the phantom, therefore favoring a strong sample/coil coupling. In this context, the plots of that study suggest that at a 6 cm depth (chosen for the discussion here as it is the radius of the phantom in the presented study), individual channels would generate about  $0.3 \mu\text{T}/\sqrt{W}$  (for a single transmitting element). The results presented in this analysis indicate approximately the same efficiency at the hot spot of  $|B_1^+|$  in the phantom for the circular patch antenna and a lower efficiency for the interdigitated capacitor probe array.

## VI. INHOMOGENEOUS IMAGING VOLUMES

The  $|B_1^+|$  field distribution is difficult to homogenize if the imaging volume is uniform. For example, the simple and symmetric cylindrical shape of the water phantom supports high-order resonant modes, increasing the spatial variation. The overall large electrical size of the phantom leads to lower maximum efficiency as the field is distributed over the entire volume. Although useful for simulation validation, a uniform phantom does not accurately describe inhomogeneous human tissues and this effect is more pronounced with higher field systems.

In this section, measurement results for two inhomogeneous phantoms of irregular shape are shown: a NIST standardized system phantom and a pineapple, which is roughly the size of a human head. The phases of the excitations for both inhomogeneous volumes are shown in Table IX with the

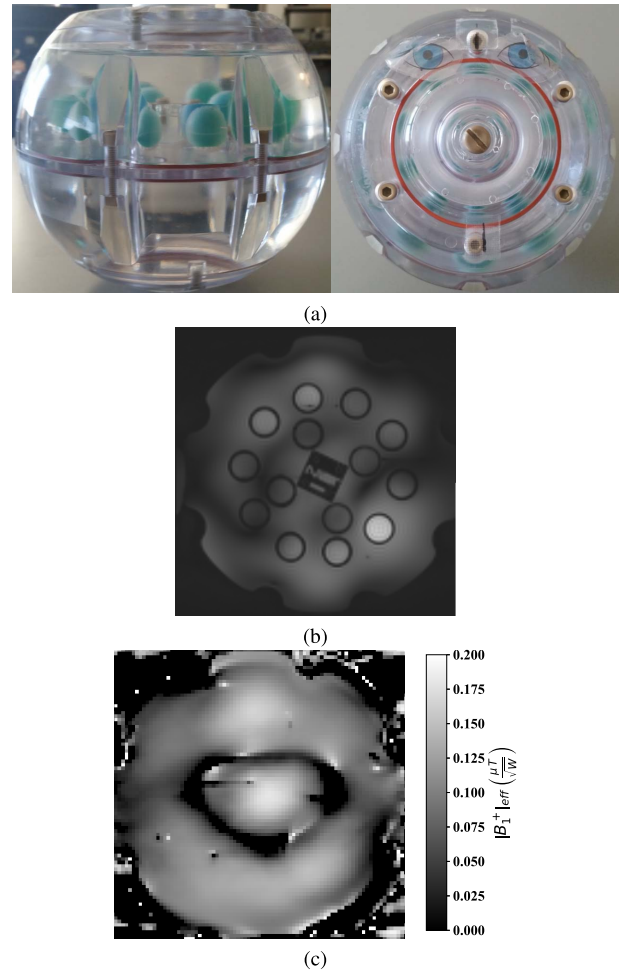


Fig. 15. Measured NIST standardized system phantom. (a) Cross sections showing the different spheres of materials, (b) GRE image, and (c) flip angle (degree scale) and corresponding efficiency map ( $\mu\text{T}/\sqrt{W}$ ).

magnitudes equal across all of the excited ports. The two circular patch ports are excited at  $163^\circ$  and  $280^\circ$ . This is slightly off quadrature to account for the imperfect circular polarization of the interdigitated capacitor probe array. These excitations are determined by optimizing the field excitation in the outer regions of the pineapple, since the high-water content core overpowers the outer regions.

The NIST standardized phantom [Fig. 15(a)] contains various spheres of materials with different T1 and T2 weightings, such that each sphere should appear with different brightness in the resulting GRE image, as shown in Fig. 15(b). The efficiency is slightly higher than the cylindrical phantom results [Fig. 15(c)] partially due to the smaller size of the phantom.

Fruit is often imaged in MRI systems due to similar electrical properties as human tissues and inhomogeneity of the internal structure. A pineapple was chosen as it is a similar size and structure to the human head. The pineapple is 15 cm long and 11 cm in diameter. Fig. 16(a) shows high-resolution details of all parts of the pineapple, while Fig. 16(b) shows significantly more field excited toward the high-water content center core. Only one cross section for both inhomogeneous

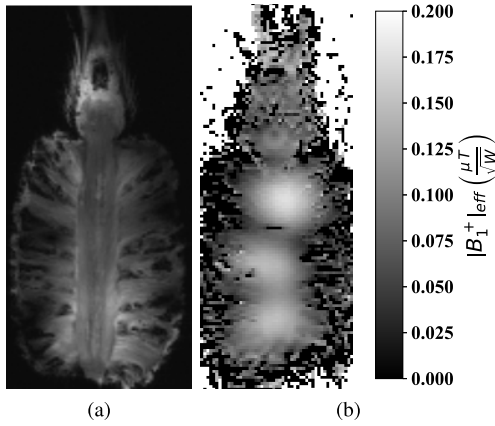


Fig. 16. Measured pineapple. (a) GRE image and (b) flip angle (degree scale) and corresponding efficiency map ( $\mu\text{T}/\sqrt{W}$ ).

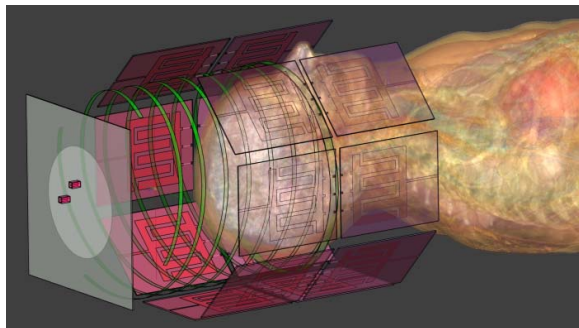


Fig. 17. Simulation setup showing an anatomically accurate human body model from the IT'IS Virtual Population, *Duke*, with the shorted undriven quadrifilar helix with circular patch probe and 14 interdigitated capacitor probes.

phantoms is shown and a similar efficiency increase is obtained for all cuts.

### VII. ANATOMICALLY ACCURATE HUMAN BODY MODEL

The various excitations described in the previous sections are next used in simulations with *Duke*, an anatomically correct adult male from the IT'IS (Zürich, Switzerland) Virtual Population v3.1 [28]. The model contains 300 bones and tissues with accurate electrical properties across frequency. The relative phasing and magnitude are optimized for the volume of the head from the bottom of the ears to the top of the skull. Normalized  $|B_1^+|$  results are shown and the 10-g SAR maps are normalized to the maximum of 3.2 W/kg specified by the IEC 60601-2-33 standard. The simulated plots show a sagittal cut in the center of the body on the right and a coronal cut in the center of the body on the left. The plots are cropped to roughly the armpits as there is no significant field below the shoulders. First, only a patch probe is simulated, then it is combined with the interdigitated capacitor probe array, and finally, an undriven helix is added, with the final combination shown in Fig. 17.

#### A. Patch Probe and Interdigitated Capacitor Probe Array

The circular patch probe is placed 17 cm from the top of the head. Fig. 18 shows the resulting excitation with poor field

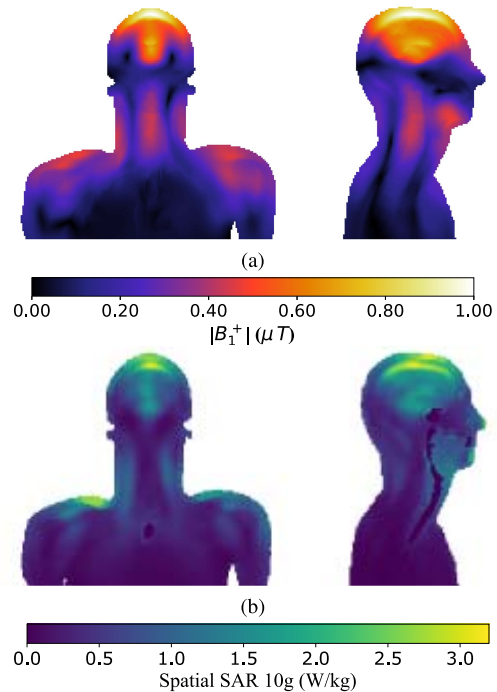


Fig. 18. Results inside the head and shoulder volume of *Duke* using the circular patch probe excitation. (a)  $|B_1^+|$ . (b) sSAR10g.

coverage; only the top and the middle of the head are excited with low-field coverage on the sides. The peak of the SAR is located in a concave region of the shoulders, which then limits the maximum field excitation in the region of interest.

The interdigitated capacitor probe array is placed such that the chin is at the lower edge of the array, so that the center of the volume excitation is aligned with the brain. The head is larger than the uniform cylindrical phantom; therefore, the excitation for *Duke* adds an array element for each row, totaling 14 excitations in the array. Top radiating elements are not used as the coverage provided by the elements is already satisfied by the circular patch probe and the elimination of the element will potentially improve patient comfort. The combination of the array and the single circular patch probe can help to improve the field coverage inside of the imaging region. The optimized excitation is shown in Table X, where the voltage excitation is normalized to the patch probe excitation. To improve the right-handed circular polarization inside of the head, with the interdigitated capacitor probe array in place, the feeding of the circular patch probe is modified so that it is no longer in quadrature. The imperfect shape of the head will affect the quality of the circular polarization, such that the coronal and sagittal cuts do not see a similar electrical structure. The lack of a top radiating element in the interdigitated capacitor probe array further complicates the excitation, requiring a combination of the sources to help maintain a circular polarized field.

Fig. 19 shows that the combination of the two excitations helps to improve the magnitude of the field in the outer regions of the head, but much of the inner regions have a low field magnitude. The combination with the interdigitated

TABLE X  
PATCH PROBE AND INTERDIGITATED CAPACITOR PROBE ARRAY  
RELATIVE MAGNITUDE AND PHASE EXCITATION  
WITH *Duke* (FIG. 19)

Patch Probe Port	Magnitude	Phase °
1	1	196
2	1	217
Interdigitated Capacitor	Magnitude	Phase °
1	1.25	13
2	2.08	63
3	2.08	86
4	2.08	111
5	2.08	181
6	2.08	262
7	2.1	328
8	1	18
9	1.62	58
10	1.45	133
11	1.18	164
12	1.67	208
13	1.68	236
14	1.76	280

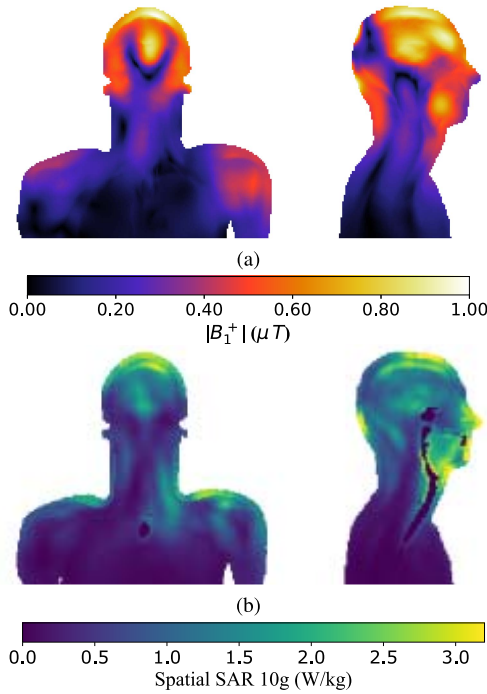


Fig. 19. Results inside the head and shoulder volume of *Duke* using the circular patch probe and interdigitated capacitor probe array excitation. (a)  $|B_1^+|$ . (b) sSAR10g.

capacitors shifts the unwanted absorption from the shoulders to the imaging region of the head. Practically, this is useful because the limiting factor of the field excitation would be the volume being imaged, as opposed to another part of the body. However, there is higher absorption at the tip of the nose which could be reduced through further optimization with explicit constraint on max SAR10g.

### B. Helix Boundary Condition

The undriven quadrifilar helix is next added with the final configuration containing all elements of Fig. 6. The helix pitch is decreased to 3 cm and the separation between the helix

TABLE XI  
PATCH PROBE AND INTERDIGITATED CAPACITOR PROBE ARRAY  
RELATIVE MAGNITUDE AND PHASE EXCITATION WITH *Duke*  
AND HELIX BOUNDARY CONDITION (FIG. 20)

Patch Probe Port	Magnitude	Phase °
1	1	32
2	1	157
Interdigitated Capacitor	Magnitude	Phase °
1	0.83	18
2	1.67	91
3	1.67	223
4	1.67	276
5	2.1	321
6	2.08	11
7	2.05	36
8	1.43	1
9	2.06	25
10	0.76	65
11	2.04	104
12	1.47	129
13	0.39	198
14	1.44	261

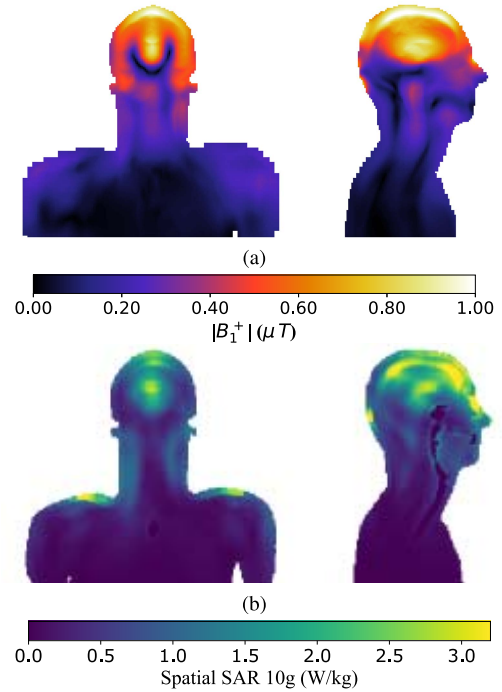


Fig. 20. Results inside the head and shoulder volume of *Duke* using the circular patch probe and interdigitated capacitor probe array excitation with shorted helix boundary condition. (a)  $|B_1^+|$ . (b) sSAR10g.

and the head remains at 1 cm. The optimized excitation is shown in Table XI with results shown in Fig. 20. The addition of the quadrifilar helix helps balance the overall magnetic field distribution in the upper region of the head. The field gradient from the outer to the inner region is reduced. With the addition of the helical boundary structure, the phase difference between the circular patch probe feeds is closer to 90° than the previous case as it helps improve on the imbalance created by an imperfect volume. Since the most important part of the head for ultra-high-field MRI is the brain, this approach improves the homogeneity in the region of interest. It is interesting to note that the lower portion of the head, roughly even with the nose, is still difficult to excite, but a modified excitation could

be designed for a redefined optimized region. The refocusing of the fields reduces the SAR peaks in the lower portion of the head and even in the outer regions of the head.

### VIII. CONCLUSION

In summary, this paper presents an investigation of various designs for the excitation and control of RF EM fields in a human-size 10.5-T MRI bore. Particular attention is given to methods that have the potential of improving the uniformity of the  $B_1^+$  field inside several types of phantoms. Several conclusions can be made from the simulation and measurement results presented in this paper. First, FDTD simulations using Sim4Life (Zurich MedTech) are validated by measurements on a uniform cylindrical water phantom using two different types of excitations and their combination, as well as three different passive field modifying structures. The simulated data are compared to measurements, and the measured data are quantitatively compared for various configurations. Although the homogeneous symmetrical phantom fundamentally supports resonant modes and, therefore, results in large field uniformities, it is found that a combination of a circularly polarized patch and a traveling-wave capacitively loaded probe gives the largest field homogeneity when combined with a passive quadrifilar helix and soft EM surface that both surround the phantom.

After validating the simulations with measurements for the uniform water phantom, a second set of measurements is performed on two nonuniform phantoms: a standard NIST phantom and a pineapple. Both of these phantoms lack the uniformity and symmetry of the water cylinder and show an improved  $B_1^+$  field homogeneity when the same excitation and field modifying devices are used, with a  $2.8\times$  increase in efficiency.

Finally, simulations are performed with an anatomically correct human body model from the ITIS virtual population and with the various configurations used in the measurements. The  $B_1^+$  field distribution along with field absorption (SAR<sub>10g</sub>) in the tissues of the head and shoulder region of a mature male are plotted and analyzed. The best combination of probes and passive field structures that give a more uniform and stronger  $B_1^+$  is found to be the case with the circular patch combined with the interdigitated capacitor probe with a shorted passive quadrifilar helix surrounding the head region.

In conclusion, this paper demonstrates effective simulations with various levels of imaging volume complexity, as well as validation with a number of measurements on a 10.5-T MRI system. Several techniques for improved RF field excitation and distribution are investigated and compared, showing that the desired circular-polarized transmit  $B$ -field component can be focused in specific regions by excitation phasing while maintaining a low absorption in the tissues of a human body imaging volume.

### ACKNOWLEDGMENT

The authors would like to thank Dr. A. Kiruluta from the Physics Department, Harvard University, for the help in this paper, and Dr. K. Keenan from NIST, Boulder, CO, USA, for providing the spherical phantom for measurements.

### REFERENCES

- [1] K. Haines *et al.*, "MR microimaging with a cylindrical ceramic dielectric resonator at 21.1 T," presented at the 51st ENC Exp. Nucl. Magn. Reson. Conf., Daytona Beach, FL, USA, Apr. 2010.
- [2] R. Fu *et al.*, "Ultra-wide bore 900 MHz high-resolution NMR at the national high magnetic field laboratory," *J. Magn. Reson.*, vol. 177, no. 1, pp. 1–8, 2005.
- [3] V. D. Schepkin, W. W. Brey, P. L. Gor'kov, and S. C. Grant, "Initial *in vivo* rodent sodium and proton MR imaging at 21.1 T," *Magn. Reson. Imag.*, vol. 28, no. 3, pp. 400–407, 2010.
- [4] K. Uğurbil, "Magnetic resonance imaging at ultrahigh fields," *IEEE Trans. Biomed. Eng.*, vol. 61, no. 5, pp. 1364–1379, May 2014.
- [5] B. Wu *et al.*, "Shielded microstrip array for 7 T human MR imaging," *IEEE Trans. Med. Imag.*, vol. 29, no. 1, pp. 179–184, Mar. 2010.
- [6] I. R. O. Connell, K. M. Gilbert, M. A. Abou-Khousa, and R. S. Menon, "Design of a parallel transmit head coil at 7 T with magnetic wall distributed filters," *IEEE Trans. Med. Imag.*, vol. 34, no. 4, pp. 836–845, Apr. 2015.
- [7] S.-M. Sohn, L. DelaBarre, A. Gopinath, and J. T. Vaughan, "RF head coil design with improved RF magnetic near-fields uniformity for magnetic resonance imaging (MRI) systems," *IEEE Trans. Microw. Theory Techn.*, vol. 62, no. 8, pp. 1784–1789, Aug. 2014.
- [8] B. Wu *et al.*, "Multi-channel microstrip transceiver arrays using harmonics for high field MR imaging in humans," *IEEE Trans. Med. Imag.*, vol. 31, no. 2, pp. 183–191, Feb. 2012.
- [9] A. J. Raaijmakers *et al.*, "The fractionated dipole antenna: A new antenna for body imaging at 7 tesla," *Magn. Reson. Med.*, vol. 75, no. 3, pp. 1366–1374, 2016.
- [10] P. Bluem *et al.*, "Travelling-wave excitation for 16.4 T small-bore MRI," in *Proc. IEEE MTT-S Int. Microw. Symp. (IMS)*, May 2015, pp. 1–4.
- [11] D. Brunner, N. D. Zanche, J. Frohlich, J. Paska, and K. P. Pruessmann, "Travelling-wave nuclear magnetic resonance," *Nature*, vol. 457, no. 7232, pp. 994–998, Feb. 2009.
- [12] J. Hoffmann, G. Shajan, J. Budde, K. Scheffler, and R. Pohmann, "Human brain imaging at 9.4 T using a tunable patch antenna for transmission," *Magn. Reson. Med.*, vol. 69, no. 5, pp. 1494–1500, 2013.
- [13] G. Shajan, J. Hoffmann, D. Z. Balla, D. K. Deelchand, K. Scheffler, and R. Pohmann, "Rat brain MRI at 16.4 T using a capacitively tunable patch antenna in combination with a receive array," *NMR Biomed.*, vol. 25, no. 10, pp. 1170–1176, 2012.
- [14] A. Andreychenko, H. Kroeze, V. O. Boer, J. J. W. Lagendijk, P. R. Luijten, and C. A. T. van den Berg, "Improved steering of the RF field of traveling wave MR with a multimode, coaxial waveguide," *Magn. Reson. Med.*, vol. 71, no. 4, pp. 1641–1649, 2014.
- [15] M. A. Ertürk *et al.*, "Toward imaging the body at 10.5 tesla," *Magn. Reson. Med.*, vol. 77, no. 1, pp. 434–443, 2017.
- [16] NIST. *ISMRM/NIST System Phantom*. Accessed: Oct. 28, 2016. [Online]. Available: <http://www.hpd-online.com/system-phantom.php>
- [17] S. Ramo, J. R. Whinnery, and T. Van Duzer, *Fields and Waves in Communication Electronics*. Hoboken, NJ, USA: Wiley, 1994, ch. 8, p. 430.
- [18] V. L. Yarnykh, "Actual flip-angle imaging in the pulsed steady state: A method for rapid three-dimensional mapping of the transmitted radiofrequency field," *Magn. Reson. Med.*, vol. 57, pp. 192–200, Jan. 2007.
- [19] P.-F. Van de Moortele, C. Snyder, L. DelaBarre, G. Adriany, J. Vaughan, and K. Ugurbil, "Calibration tools for RF shim at very high field with multiple element RF coils: From ultra fast local relative phase to absolute magnitude B1+ mapping," *Int. Soc. Magn. Reson. Med.*, vol. 15, p. 1676, Apr. 2007.
- [20] P. F. Van de Moortele and K. Ugurbil, "Very fast multi channel B1 calibration at high field in the small flip angle regime," in *Proc. 17th Annu. Meeting Int. Soc. Magn. Reson. Med.*, Honolulu, HI, USA, Apr. 2009, p. 367.
- [21] G. J. Metzger *et al.*, "Dynamically applied B1+ shimming solutions for non-contrast enhanced renal angiography at 7.0 tesla," *Magn. Reson. Med.*, vol. 69, no. 1, pp. 114–126, 2013.
- [22] P. Bluem, A. Kiruluta, P.-F. Van de Moortele, A. Duh, G. Adriany, and Z. Popović, "Patch-probe excitation for ultrahigh magnetic field wide-bore MRI," *IEEE Trans. Microw. Theory Techn.*, vol. 65, no. 7, pp. 2547–2557, Jul. 2017.
- [23] A. Munir and E. K. Sari, "Printed traveling wave antenna composed of interdigital capacitor structure for wireless communication application," in *Proc. Int. Seminar Intell. Technol. Appl. (ISITIA)*, May 2015, pp. 441–444.

- [24] Y. M. Madany, D. A. Mohamed, and B. I. Halim, "Analysis and design of microstrip antenna array using interdigital capacitor with CRLH-TL ground plane for multiband applications," in *Proc. 8th Eur. Conf. Antennas Propag. (EuCAP)*, Apr. 2014, pp. 922–926.
- [25] R. Schmidt and A. Webb, "Improvements in RF shimming in high field MRI using high permittivity materials with low order pre-fractal geometries," *IEEE Trans. Med. Imag.*, vol. 35, no. 8, pp. 1837–1844, Aug. 2016.
- [26] G. Ruvio, P. S. Kildal, and S. Maci, "Modal propagation in ideal soft and hard waveguides," in *Proc. IEEE Antennas Propag. Soc. Int. Symp.*, vol. 4, Jun. 2003, pp. 438–441.
- [27] E. Lier and P.-S. Kildal, "Soft and hard horn antennas," *IEEE Trans. Antennas Propag.*, vol. AP-36, no. 8, pp. 1152–1157, Aug. 1988.
- [28] M.-C. Gosselin *et al.*, "Development of a new generation of high-resolution anatomical models for medical device evaluation: The virtual population 3.0," *Phys. Med. Biol.*, vol. 59, no. 18, p. 5287, Aug. 2014.

**Patrick Bluem** (S'14–GS'14) received the B.S. and M.S. degrees in electrical engineering from the University of Colorado, Boulder, CO, USA, in 2014 and 2016, respectively, where he is currently pursuing the Ph.D. degree under Z. Popović.



**Pierre-Francois Van de Moortele** received the Ph.D. degree with a focus on acquisition methods for fast imaging on a 3-T system from the University of Paris Sud (Paris XI), Paris, France, in 1999.

He has been involved in magnetic resonance imaging (MRI) methods in humans with a focus on scanners operating at high (3 T) and ultra-high (7 T) magnetic fields. He was with the Center for Magnetic Resonance Research (CMRR), University of Minnesota, Minneapolis, MN, USA, where he was involved in the research at 7 and 9.4 T, developing

multiple approaches to address transmit  $B_1$  heterogeneity in multichannel head and body transmit RF arrays for a large range of human applications, especially cardiovascular and cerebral targets. He is currently an Associate Professor with CMRR, where he is involved in the investigation of transmit  $B_1$  issues on a 10.5-T system, which is currently the largest available whole-body human MR scanner. He has co-authored more than 100 peer-reviewed articles related with MRI.



**Gregor Adriany** (M'14) received the M.S. and Ph.D. degrees in electrical engineering from RWTH Aachen University, Aachen, Germany.

He is currently an Associate Professor with the Center for Magnetic Resonance Research, University of Minnesota, Minneapolis, MN, USA. He was involved in high-frequency design, particularly related to magnetic resonance imaging coils and antennas and his pioneering work related to ultra-high-field (UHF) transmit arrays at 7, 9.4, and 10.5 T resulted in numerous highly cited publications. His current research interests include optimized antenna and technology development for UHF human MRI applications at 7 and 10.5 T.



**Zoya Popović** (S'86–M'90–SM'99–F'02) received the Dipl.Ing. degree from the University of Belgrade, Belgrade, Serbia, and the Ph.D. degree from the California Institute of Technology, Pasadena, CA, USA.

From 2001 to 2003, she was a Visiting Professor with the Technical University of Munich, Munich, Germany. In 2014, she was a Visiting Professor with ISAE, Toulouse, France. She is currently a Distinguished Professor and the Lockheed Martin Endowed Chair of Electrical Engineering with the University of Colorado, Boulder, CO, USA. She holds a Chair of Excellence with Carlos III University, Madrid, Spain, in 2018/2019. She has graduated 58 Ph.D. students and currently advises 14 doctoral students. Her current research interests include high-efficiency power amplifiers and transmitters, microwave and millimeter-wave high-performance circuits for communications and radar, medical applications of microwaves, and wireless powering.

Dr. Popović was as a Foreign Member of the Serbian Academy of Sciences and Arts in 2006. She was the IEEE MTT-S Distinguished Educator in 2013 and the University of Colorado Distinguished Research Lecturer in 2015. She was a recipient of the two IEEE MTT Microwave Prizes for best journal papers, the White House NSF Presidential Faculty Fellow Award, the URSI Issac Koga Gold Medal, the ASEE/HP Terman Medal, and the German Humboldt Research Award.